This Supplementary Information file replaces the version that was published on 8 June 2021, which contained an error on page S7. When describing equation S1, it was originally stated that:

"A unitary Löwdin transformation was implemented to convert H_0 into a Hamiltonian, H, in an orthogonal basis set via the following equation:"

The Löwdin transformation is not unitary and the correct sentence is provided in this revised file. It reads as follows:

"A Löwdin transformation was implemented to convert H_0 into a Hamiltonian, H, in an orthogonal basis set via the following equation:"

The authors apologise for this error and any consequent inconvenience.

Supplementary Information

Role of Intercalation on Electrical Properties of Nucleic Acids for use in Molecular Electronics

Hashem Mohammad[a,#], Busra Demir[b,c,#], Caglanaz Akin[b,c], Binquan Luan[d], Joshua Hihath[e], Ersin Emre Oren[b,c,*], and M. P. Anantram[a,*]

[a]Department of Electrical Engineering, University of Washington, Seattle, WA, USA. [b]Bionanodesign Laboratory, Department of Biomedical Engineering, TOBB University of Economics and Technology, Ankara, Turkey. [c]Department of Materials Science & Nanotechnology Engineering, TOBB University of Economics and Technology, Ankara, Turkey. [d] Computational Biological Center, IBM Thomas J. Watson Research, Yorktown Heights, NY 10598, USA. [e]Electrical and Computer Engineering Department, University of California Davis, Davis, CA, USA.

[#] *These authors contributed equally.*

*E-mails: eeoren@etu.edu.tr, anantmp@uw.edu

Table of Contents

Methods

To investigate the electronic properties, we first use MD simulations to obtain representative structures, followed by DFT calculations to generate the system Hamiltonian that contains energy level information and their coupling. In the third step, we use the Hamiltonian in a Green's function method with Büttiker probes to calculate the conductance.

Molecular Dynamics We opted to use both CHARMM and AMBER to study the effect of intercalation on the nucleic acid structure from two different starting points. However, as the DFT results and charge transport calculations will show, the intercalation yields similar effects regardless of the MD package (force field) used.

ds-DNA and Anthraquinone We simulate the ds-DNA-Aq structures (15 base-pair or 9 base-pair long) using NAMD software[S1] and the MD was carried out using Charmm36 force field.[S2] The structure is first solvated in 0.1 M KCl electrolyte that measures 78 Å×78 Å×78 Å. The TIP3P[S3] and the standard ion[S4] force fields are used for water and KCl. A smooth cutoff (10-12 Å) is used to calculate van der Waals potential energies. Electrostatic interactions are computed using the particle-mesh Ewald (PME) method [S5] (grid size ~ 1 Å). With the SETTLE algorithm[S6] applied to keep all bonds rigid, the simulation time-step is 2 fs.

After the minimization, the entire simulated system is first equilibrated for 1 ns at 1 bar and 300 K, with all backbone atoms in the ds-DNA and non-hydrogen atoms in the anthraquinone molecule harmonically restrained (spring constant k=1 kcal/mol/Å^2). In the subsequent production simulation, the restraint is removed. The Langevin dynamics is applied to keep constant temperature (300 K) in the simulated system and the pressure is also kept constant at 1 bar using the Nosé-Hoover method.[S7] After about ~80-ns equilibration (Figure S1 and S2), a snapshot is taken of the system and minimized prior to the DFT calculations. The results of MD simulation are found to yield parallel anthraquinone intercalation between adjacent DNA base-pairs, a finding consistent with literature.[S8–S10]
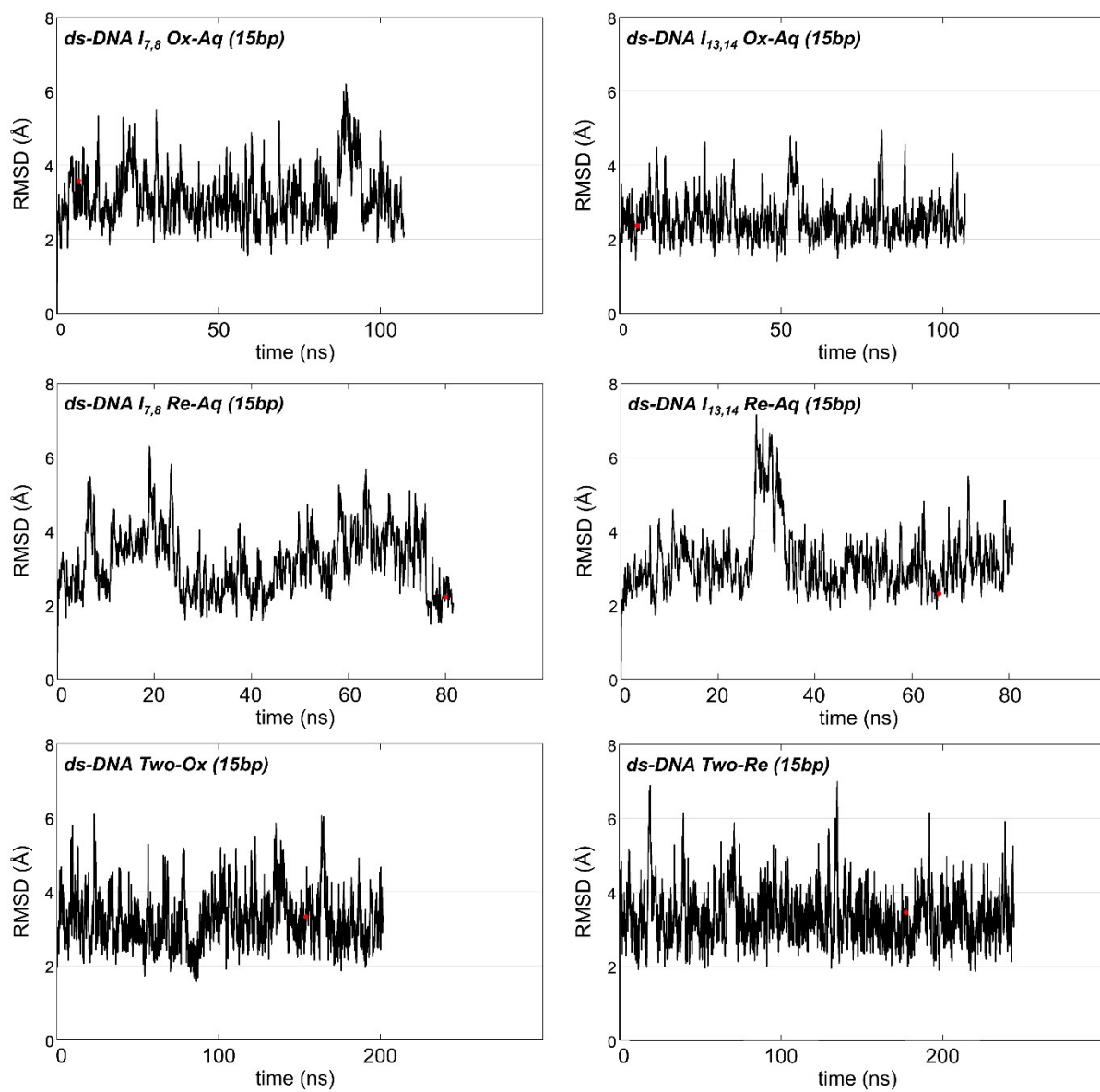
Figure S1. MD simulation RMSD plots for 15 bp ds-DNA cases. Structures chosen for DFT calculations are shown in red dot on each graph.
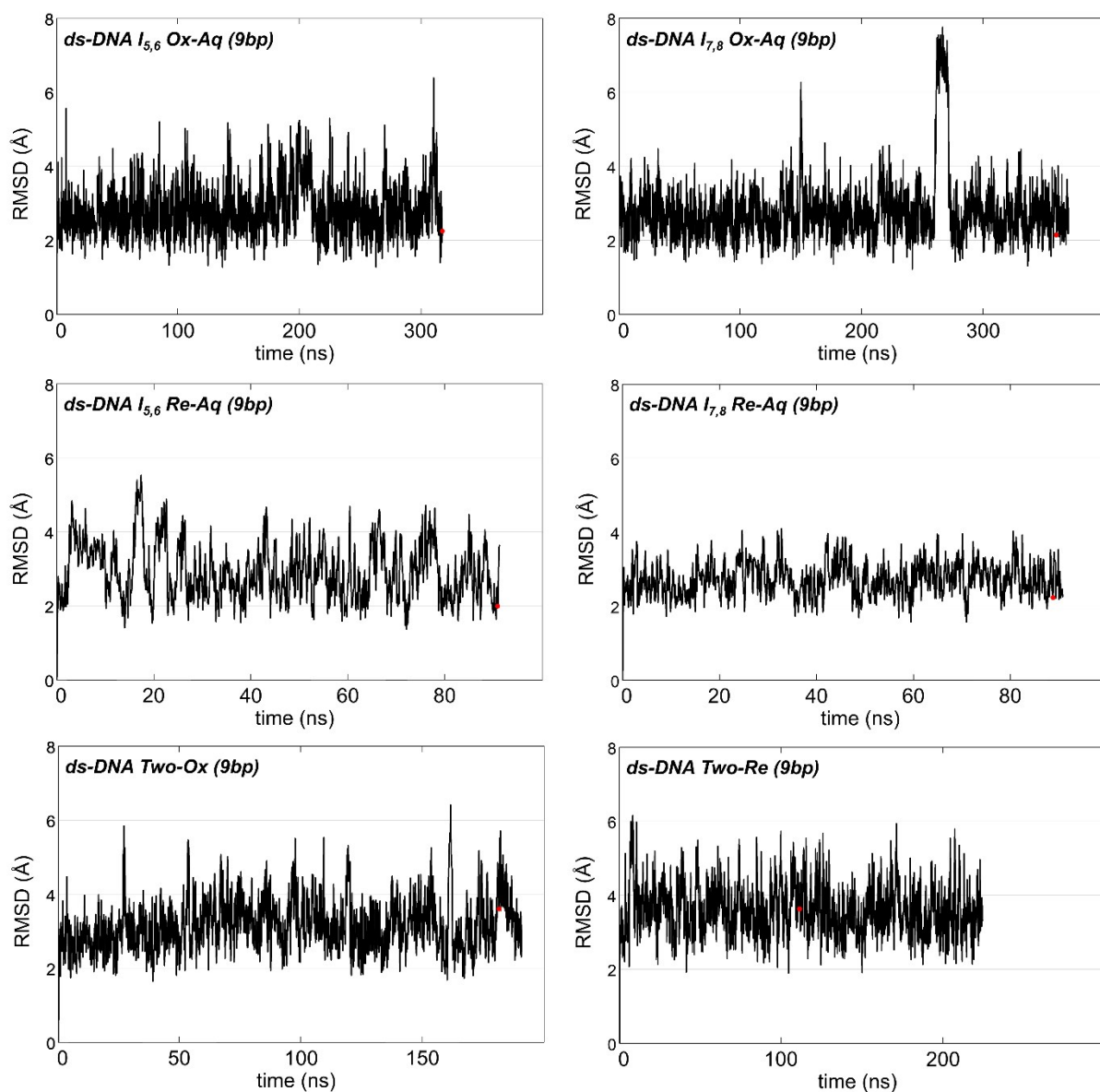
Figure S2. MD simulation RMSD plots for 9 bp ds-DNA cases. Structures chosen for DFT calculations are shown in red dot on each graph.

DNA:RNA and AqNEO We simulate the 15 base pairs DNA:RNA hybrid structure using AMBER[S11,S12] software package. We apply ff99OL3[S13,S14] and Bsc1[S15] force fields for the RNA and DNA strands, respectively. The structure is solvated with a 10 Å cutoff of TIP3P[S3] water in an octahedral periodic box and 28 Na^{+} counterions are used to neutralize the system. The SHAKE

algorithm[S16] is used to constrain all bonds with hydrogen and PME method[S5] is used for long range electrostatic interactions.

After the minimization, with a 3 Kps^{-1} heating rate, the system is heated to 300 K and then the water molecules and counterions are equilibrated for 50 ps while the DNA:RNA structure is kept restrained with a force of 25 kcal/mol. In the subsequent production simulation, the whole system is simulated for 52.5 ns with 2 fs time step. A representative structure from MD simulation is determined by RMSD based clustering algorithm within VMD software,[S17] which categorizes the conformations of the DNA:RNA hybrid observed over the course of the simulation. We choose a cutoff value of 1.75 Å RMSD to cluster the structures, selecting only nucleic part of the whole system within the 50 ns trajectory (Figure S3). The DNA:RNA hybrid having minimum RMSD value compared with the other structures within the most populated group (Figure S4) is named as the center of the top cluster (CTC) and then this representative structure is chosen and minimized before the DFT calculations.
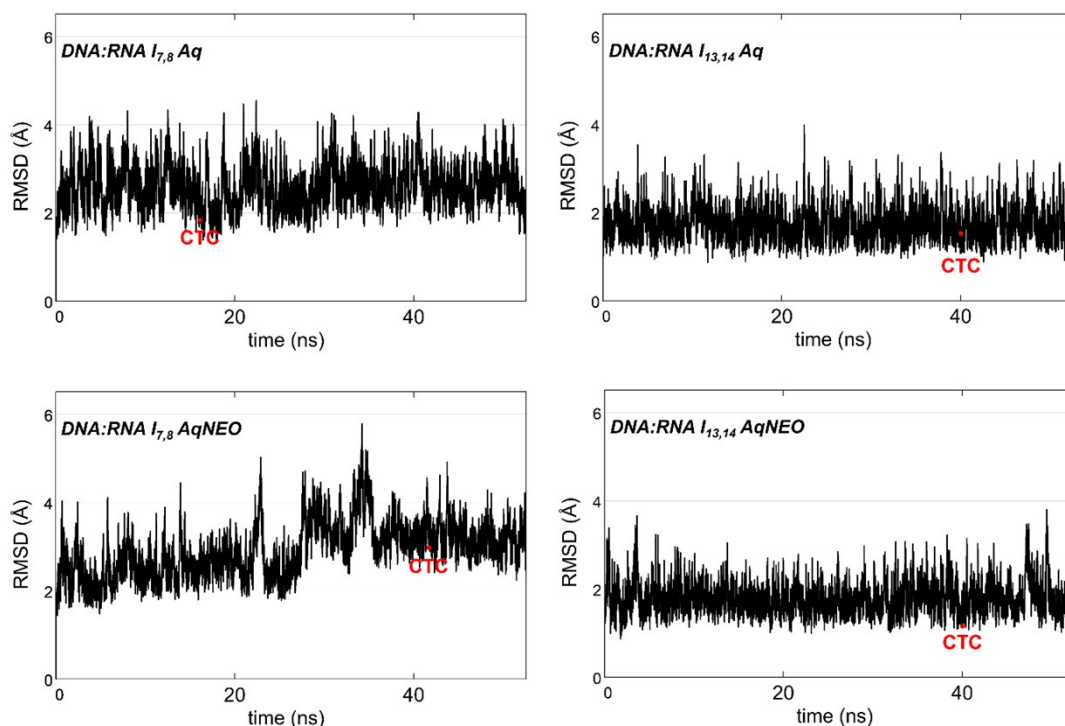

Figure S3. MD simulation RMSD plots for DNA:RNA case. Representative structures (CTC) chosen for DFT calculations are shown in red dot on each graph.

Since nucleic acid intercalator association process can take up to microseconds, we have generated the intercalated DNA:RNA structures before running MD simulations. AqNEO is placed between different base pairs of DNA:RNA structure by decreasing the distance gradually between intercalator and DNA:RNA. In every 1 Å step, local minimization is performed on both intercalator region of DNA:RNA and the intercalator itself. Then, we simulate the intercalated structures using the same minimization, heating, equilibrium, MD and structure clustering procedure with 22 Na^+ counterions due to the extra +6 charge on AqNEO. To define AqNEO molecule, GAFF[S18] force field is used and the partial charges are generated using Avogadro.[S19]
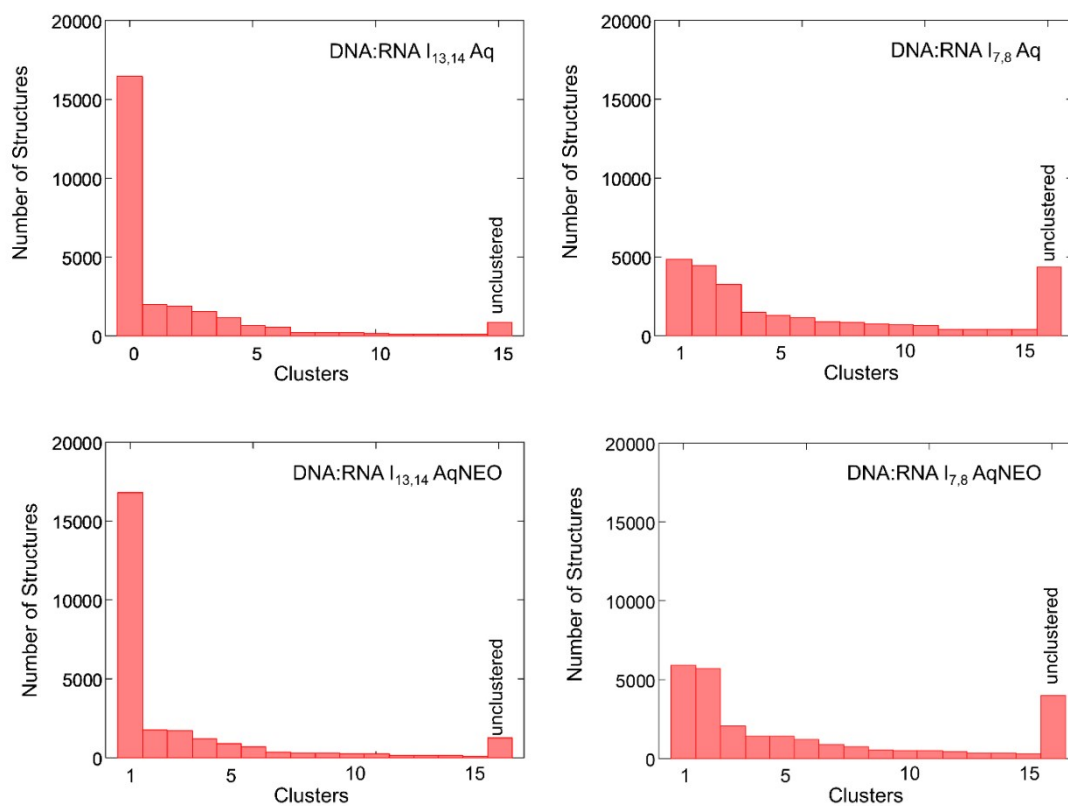

Figure S4. Cluster size distributions for DNA:RNA simulations.

DFT For the next step, the water molecules and counterions are removed from the system snapshot (for DFT convergence) and DFT calculations are then carried out using Gaussian 16 [S20] with B3LYP/6-31G(d,p) basis set. To account for water solvent effect, we use the polarizable continuum model (PCM). Furthermore, since the counterions that neutralize the DNA backbone are removed from this calculation, the total charge is set equal to the number of phosphate groups

in the system, which is -28 (the terminal bases do not include their phosphate groups). The total charge for the ds-DNA system is set to -28 for both bare and intercalated cases. For the DNA:RNA system, the total charge is set to -28 for the bare system and for the intercalated case it is set to -22 due to the total charge of +6 on the AqNEO. After reaching convergence, the Hamiltonian from the DFT results is used for charge transport calculations.

Charge Transport Calculations The calculations are carried out using the Green's function method with Büttiker probes to model phase decoherence. [S21] The main condition in this model is that the probe current at each energy is equal to zero. Hence, the electron does not gain nor lose energy while traversing the system. The calculation is set up as follows: since the DNA strand in STM-BJ methods comes into contact with gold *via* the thiol linker groups at its two ends, we assume contact locations to be at the guanines in 3'-end and 5'-end. The contact self-energy is set at a portion of the backbone of the leftmost and rightmost guanine bases (Figure 1c, Figure S8). We set the left (right) contact scattering rate Γ_L (Γ_R) to 100 meV, which resembles strong contact-molecule coupling. The decoherence scattering rate Γ_{BP} is set at 10 meV. These values are found to be within the acceptable range. [S21,S22] The calculations are carried out at room temperature, $k_B T = 0.0259\ eV$. The decoherence probes are applied to each atom in the DNA system.

To obtain the Hamiltonian, H_0, and overlap matrices, S_0, we used B3LYP/6-31G(d,p) as basis set and the system's dielectric constant is taken as 78.39, representing water. A Löwdin transformation was implemented to convert H_0 into a Hamiltonian, H, in an orthogonal basis set via the following equation:

$$H = S_0^{\frac{1}{2}} H_0 S_0^{\frac{1}{2}}$$
(S1)

Here, the diagonal elements of H represent the energy levels at each atomic orbital, and the off-diagonal elements correspond to the coupling between the different atomic orbitals. The transmission through the molecule is then calculated using Green's function method. To account for decoherence, the Büttiker-probe formalism [S21] was implemented. The retarded Green's function (G^r) is found by solving the following equation:

$$\left[E - \left(H + \Sigma_L + \Sigma_R + \Sigma_B \right) \right] G^r = I$$
(S2)

where E is the energy level, and H is the Hamiltonian defined in Eq. S1, and $\Sigma_{L(R)}$ is the left (right) contact self-energy, representing the coupling strength of the DNA to the left (right) contacts by which charge enters and leaves the DNA. The self-energy of the phase breaking Büttiker probe is defined as Σ_B, which also represents the coupling strength between the DNA and the Büttiker probes.

Regarding the self-energy of the contacts, the wide-band limit approximation is used, which ignores the real part of the matrices and treats them as energy independent parameters. This approximation stands when the DOS is almost a constant throughout the metal, which is true for gold. [S23] Thus, it is defined as $\Sigma_{L(R)} = -i\Gamma_{L(R)}/2$, and is treated as an energy-independent coupling parameter, i is the imaginary unit, and $\Gamma_{L(R)} = 100$ meV. The Büttiker probes self-energy is defined in a similar manner, as $\Sigma_B = \sum_i (-\frac{i\Gamma_i}{2})$, where subscript i represents the ith probe, and Γ_i represents the coupling strength between the probe and the coherent system, also taken as an energy-independent parameter of value $\Gamma_i = 10\ meV$. Noting here that the Büttiker probes are added to the energy levels at the atomic orbitals of each block of atoms (as per the definition of diagonal elements of H). In the low-bias region, the current at the ith probe is

$$I_i = \frac{2q}{h}\sum_{j=1}^{N}\int_{-\infty}^{+\infty}T_{ij}(E)[f_i(E)-f_j(E)]dE = \int_{-\infty}^{+\infty}J_i(E)dE$$
(S3)

$$I_i = \frac{2e}{h}\sum_{j=1}^{N}T_{ij}(\mu_i-\mu_j), \qquad i = 1,2,3,...,N$$
(S4)

where $T_{ij} = \Gamma_i G^r \Gamma_j G^a$ is the transmission probability between the ith and j^{th} probes, and $G^a = (G^r)^\dagger$ is the advanced Green's function, $f_i(E) = \left(1 + exp(\frac{E-E_{fi}}{kT})\right)^{-1}$ is the Fermi distribution, and $J_i(E)$ is the current density in probe i.

The current with respect to energy at each Büttiker probe should be zero, $J_i(E) = 0$, this yields N_b independent equations from which the following relation can be derived

$$\mu_i - \mu_L = \left(\sum_{j=1}^{N_b}W_{ij}^{-1}T_{jR}\right)(\mu_R-\mu_L), \qquad i = 1,2,3,...,N_b$$
(S5)

Here, W_{ij}^{-1} is the inverse of $W_{ij} = (1 - R_{ii})\delta_{ij} - T_{ij}(1 - \delta_{ij})$, where R_{ii} is the reflection probability at probe i, and is given by $R_{ii} = 1 - \sum_{i \neq j}^{N} T_{ij}$. And since the currents at the left (I_L) and right (I_R) contacts are not zero, because they are governed by the conservation of electron number, $I_L + I_R = 0$. This yields the equation for the current at the left contact as

$$I_L = \frac{2e}{h} T_{eff}(\mu_L - \mu_R).$$

(S6)

Comparing Eq. S4 to Eq. S6 yields effective transmission term as

$$T_{eff} = T_{LR} + \sum_{i=1}^{N_b}\sum_{j=1}^{N_b} T_{Li} W_{ij}^{-1} T_{jR}.$$

(S7)

In Eq. S7, T_{LR} is the coherent transmission from the left electrode to the right electrode. The second term is the decoherence contribution into the transmission *via* Büttiker probes. The zero-bias conductance as a function of Fermi energy is calculated as

$$G(E_f) = \frac{2q^2}{h} \int dE\, T_{eff}(E) \frac{\partial f(E - E_f)}{\partial E}$$

(S8)

and the density of states (DOS) can also be calculated *via*

$$DOS(E) = -\frac{1}{\pi} \sum Im\left(diag\left(G^r(E)\right)\right)$$

(S9)

From Eq. S6, the zero bias conductance can be approximated as $G = G_0 T_{eff}$, where the quantum conductance, G_0, can be calculated as $G_0 = \frac{2q^2}{h} \approx 7.75x10^{-5}\Omega^{-1}$.

Modeling of charge transport through nucleic acids in the contact-molecule-contact system had initially started as coherent based tunneling transport. Within that limit, the Landauer-Büttiker formalism was the prominent approach to calculate the coherent transport properties.[S24–26] These papers could not explain experiments with electrical contacts with sufficient accuracy but they include all coherent processes allowed by the Hamiltonian. Reference[S21] included decoherence phenomenologically using decoherence probes to explain experiments across four different DNA strands. We use this approach in this paper. The use of these probes includes a sequential component to the transport. In fact, the underlying Green's function approach has been used

successfully to describe devices in both the coherent and sequential limits. Some of these methods have been adopted by the semiconductor industry in modeling devices with feature sizes of 10 nm. For the case of DNA transport, we note that these models do include tunneling, superexchange and sequential components. However, we feel that it may be necessary to include the effect of the environment in a non-perturbative manner, but this has proved challenging for realistic systems.

RMSD Analysis

The structural differences between the bare ds-DNA and the intercalated cases (Figure S5a) and bare DNA:RNA and the intercalated cases (Figure S5b) have been analyzed using RMSD[S17]. The effect of $I_{7,8}$ intercalation on DNA:RNA molecular structure is given in Figure S6 as an example.
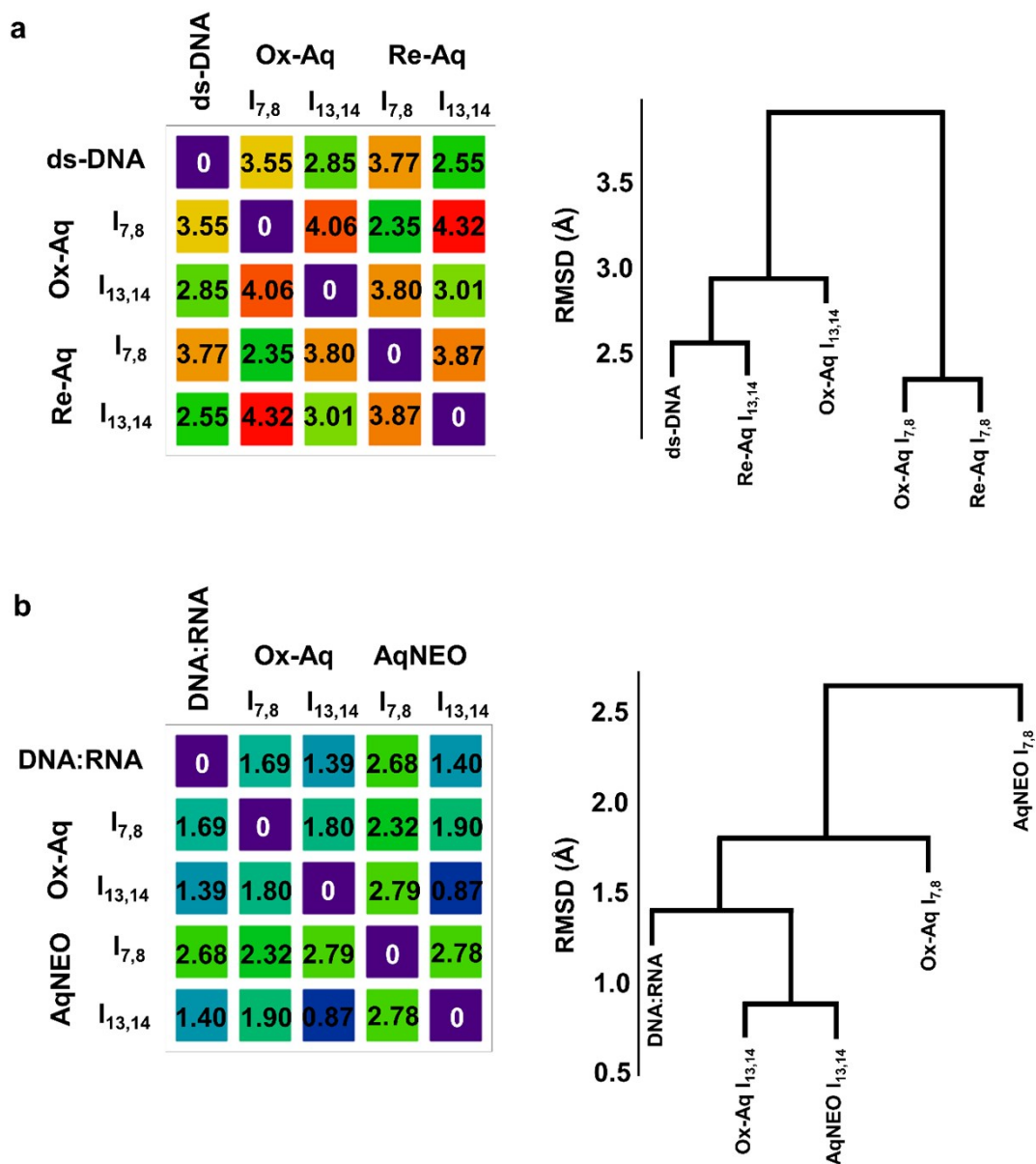

Figure S5. RMSD values and dendrograms showing the relation between each case. a) ds-DNA and intercalated cases, b) DNA:RNA and intercalated cases.
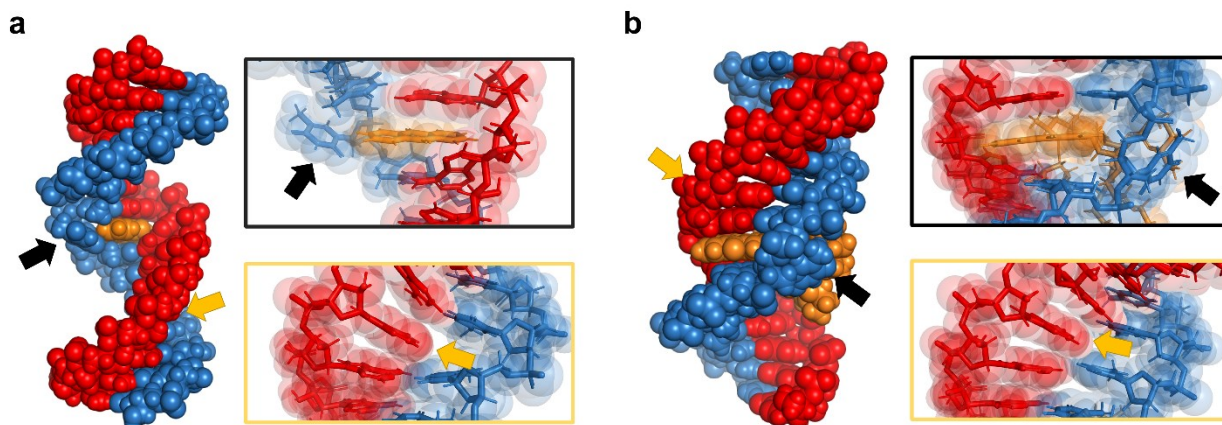
Figure S6. Structural changes in DNA:RNA $I_{7,8}$ cases. Black arrow represents the base flip out and yellow arrow represents base pair sliding for **a,** $I_{7,8}$ Ox-Aq, **b,** $I_{7,8}$ AqNEO.

Binding Energy Calculations

As the exact location of intercalations are difficult to identify both in experiments and simulations, one way to measure the more plausible location of intercalation is by computing its binding energy to DNA:RNA. Here, we computed the binding energy for the DNA:RNA system with AqNEO and with Ox-Aq *via* MMGBSA[S27] method. We assumed the conformational changes in DNA:RNA hybrid and intercalator during binding process would yield similar energy changes for each case. Thus, we compared the binding energy results and observed that through the middle of the structure ($I_{7,8}$), both AqNEO and Ox-Aq bind slightly stronger to the DNA:RNA hybrid compared to the end-location ($I_{13,14}$) (Table S1). However as seen in the main text, we did not observe significant difference in transmission plots upon changing the location of the intercalator for both cases (AqNEO and Ox-Aq).

Table S1. Binding Energy of the AqNEO and Ox-Aq into the DNA:RNA structure

Structure	Binding Free Energy (kcal/mol)
$I_{13,14}$ AqNEO	-75.44 ± 6.84
$I_{7,8}$ AqNEO	-68.62 ± 5.92
$I_{13,14}$ Ox-Aq	-26.35 ± 1.61
$I_{7,8}$ Ox-Aq	-24.21 ± 2.04

HOMO & LUMO Plots of DNA:RNA

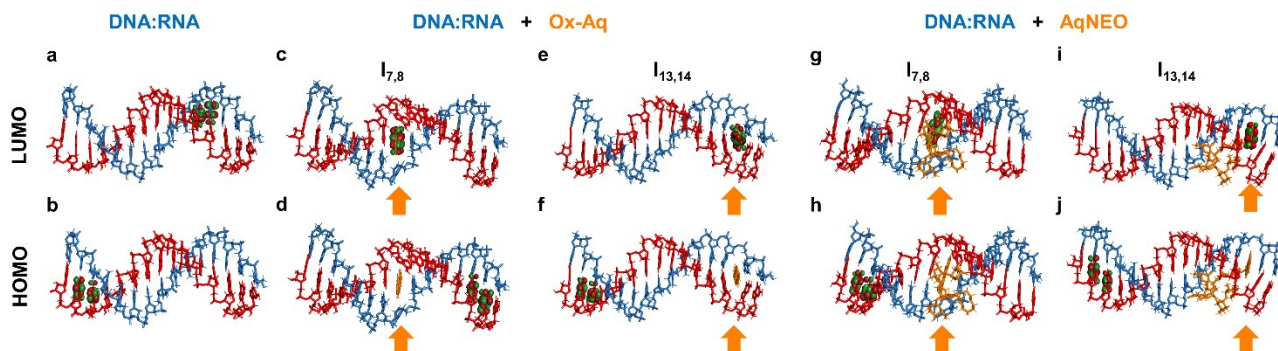The LUMO and HOMO locations are given in Figure S7 for DNA:RNA.

Figure S7. LUMO and HOMO plots both without and with Aq/AqNEO (ISO value is 0.02). **a and b,** LUMO and HOMO distribution of DNA:RNA. **c and d,** LUMO and HOMO distribution of DNA:RNA intercalated with Ox-Aq between 7th and 8th base pairs. **e and f,** LUMO and HOMO distribution of DNA:RNA intercalated with Ox-Aq between 13th and 14th base pairs. **g and h,** LUMO and HOMO distribution of DNA:RNA with same intercalation position with c and d using AqNEO. **i and j,** LUMO and HOMO distribution of DNA:RNA with same intercalation position with e and f using AqNEO.

Transmission Plots

Contacts Locations for Charge Transport Calculations

For the charge transport calculations, it is assumed that the gold electrodes are in contact with the Guanine bases located at the 3' and 5' ends of the same strand. Those atoms contacting the gold electrodes are shown in the Figure S8.

The transmission plots of the ds-DNA systems as well as the DNA:RNA systems are given in Figure S9 and Figure S10, respectively.
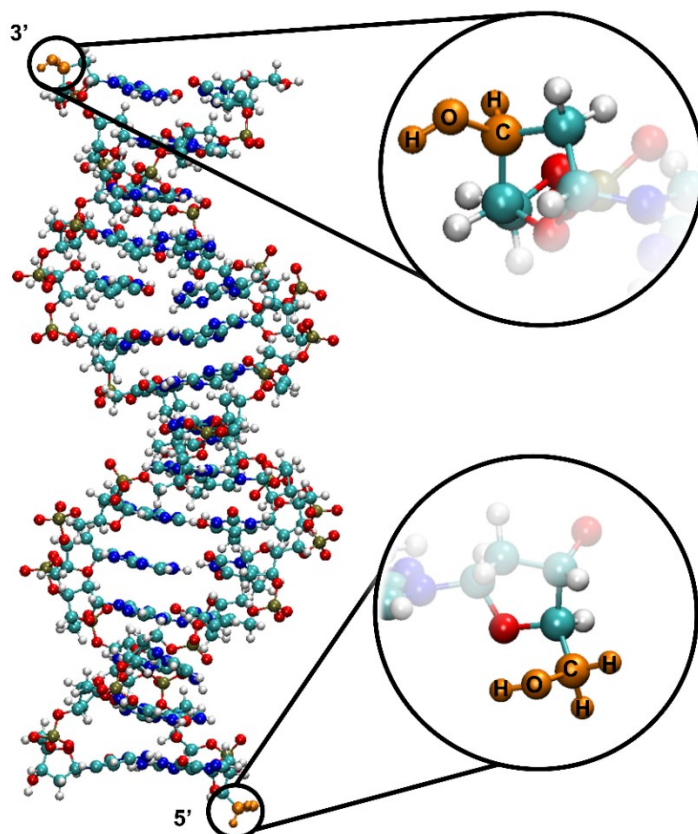
Figure S8. The contact atoms (highlighted with orange) are defined at the backbone atoms of the guanine bases located at both 3' and 5' ends of the same strand.
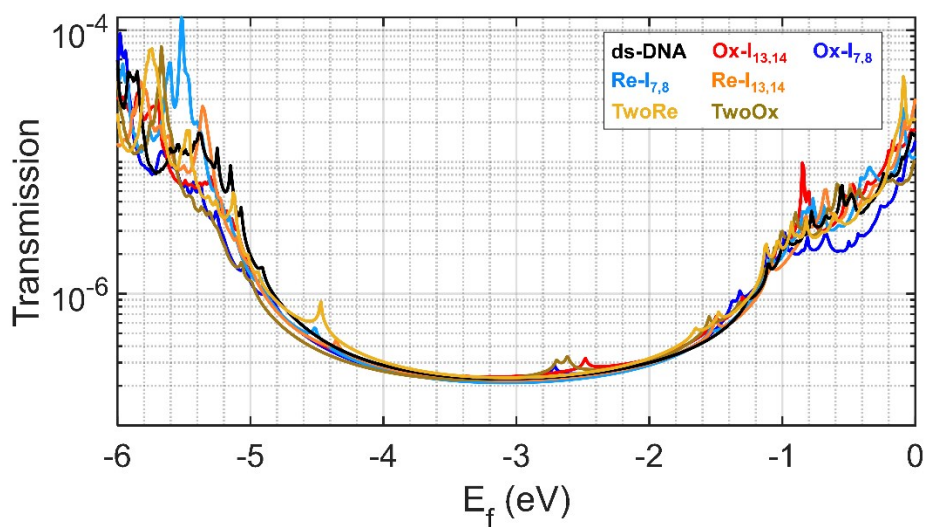

Figure S9. Transmission over a large energy window spanning HOMO and LUMO for ds-DNA 3'-G3A9G3'5'.
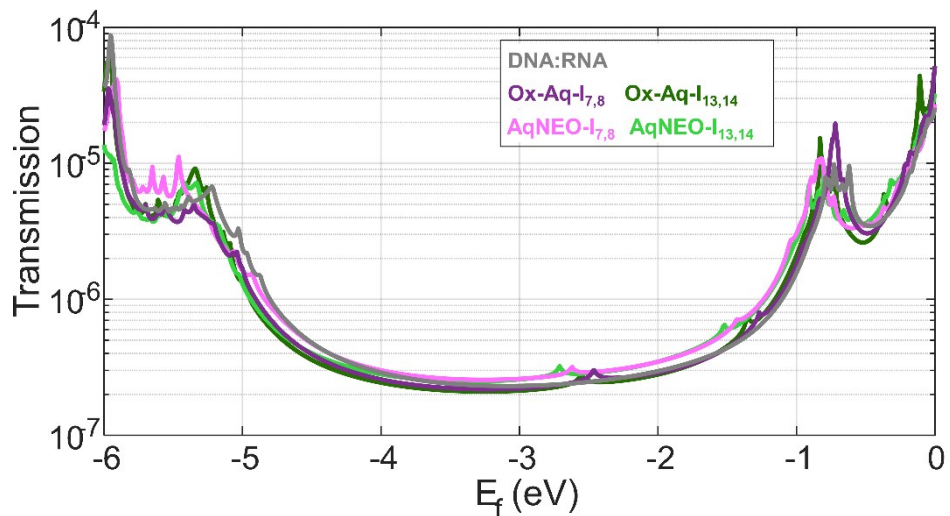
Figure S10. Transmission over a large energy window spanning HOMO and LUMO for DNA:RNA.

Comparison of the results for intercalating Aq between the 13th and 14th base-pairs (the $I_{13,14}$ case) of the ds-DNA as well as the DNA:RNA system is given in Figure S11. We notice that the induced energy level by the intercalator is very similar for both cases (80 meV shift in energy), and the transmission peaks only vary by less than 15%. The impact of intercalation on either ds-DNA or DNA:RNA systems is similar as we stated in the manuscript.
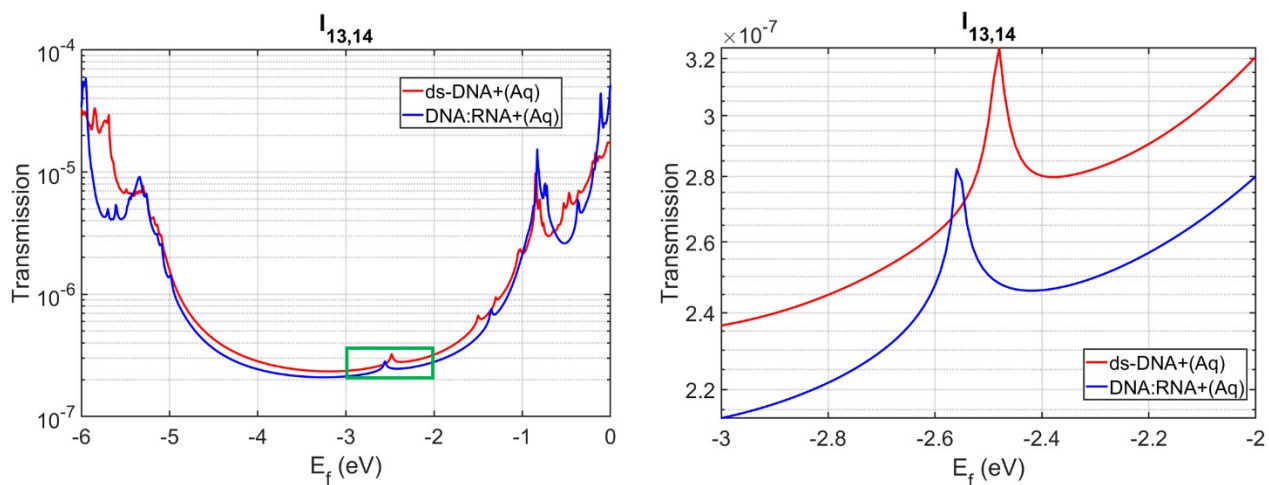

Figure S11. Transmission plot of ds-DNA and DNA:RNA systems with Aq intercalation at the $I_{13,14}$ location. Right shows the transmission peaks of the Aq-induced levels highlighted green in left figure.

Effect of Intercalation Location on Transmission

To further investigate the effect of intercalation location on the long AT region structure (ds-DNA), we focused on the charge transport mechanism induced by the intercalators by using two-step hopping scheme shown in Figure S12.

The aim of this analysis is to see the impact of distance on the transmission between Ox-Aq and the ds-DNA. The first calculation in this scheme sets the left contact location at the leftmost guanine base, while the right contact is set at the Aq. This yields the transmission probability for an electron to enter the DNA and hop into the Aq, T_1. The second calculation, T_2, assumes the left contact is at the Aq, while the right contact is set at the other end of the DNA strand, which is also a guanine. This will yield the transmission probability for an electron present at Aq to traverse the structure and exit the DNA through the other end. Then, we calculated the equivalent transmission for this system using equation S10.

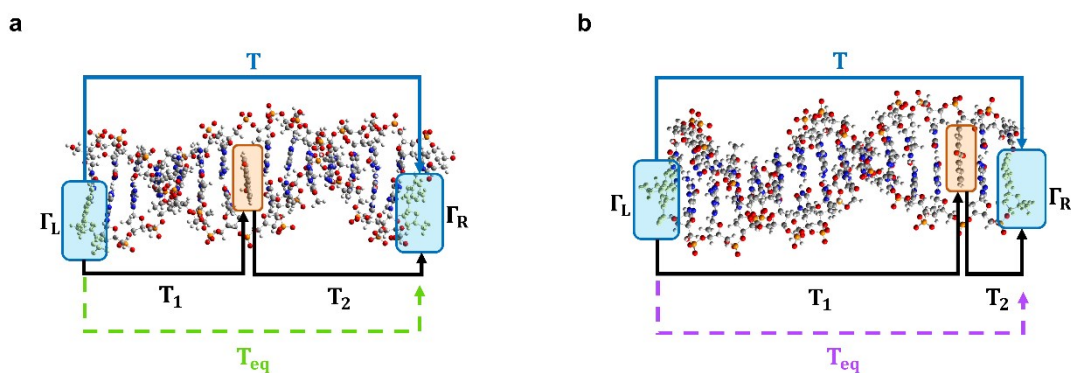$$\frac{1}{T_{eq}} = \frac{1}{T_1} + \frac{1}{T_2}$$

(S10)

Figure S12. The two-step hopping scheme for $I_{7,8}$ (**a**), $I_{13,14}$ (**b**). T_1 is the transmission from leftmost guanine to Aq. T_2 is the transmission from Aq to rightmost guanine. T is the transmission from leftmost guanine to rightmost guanine as in the total transmission from left to right, which is used in the main text. T_{eq} is the equivalent transmission calculated using Eq. S10.

The results show that the distance between contact points and intercalation molecule (thus, the intercalation location) plays a significant role in transmission unless the strand is too long to show the effect (Figure S13). As even though the second hop, T_2, is two orders of magnitude higher than

T_1 for $I_{13,14}$, the equivalent transmission is going to be lowered due to the low value of T_1. This is expected since T_2 has the right contact location (Guanine) very close to Aq (0.7 nm), while the first hop requires the electron to travel a large distance of 12 base pairs (3.68 nm) to reach the Aq which dominates the overall transmission along the system. Moreover, a similar effect is seen for the $I_{7,8}$ case where the electron must travel almost the same distance per hop, 2.38 nm and 2.72 nm for T_1 and T_2, respectively. Even though the induced energy levels for $I_{13,14}$ and $I_{7,8}$ are at different spatial locations, the equivalent tunneling through the whole molecule is weak regardless of the location of Aq.
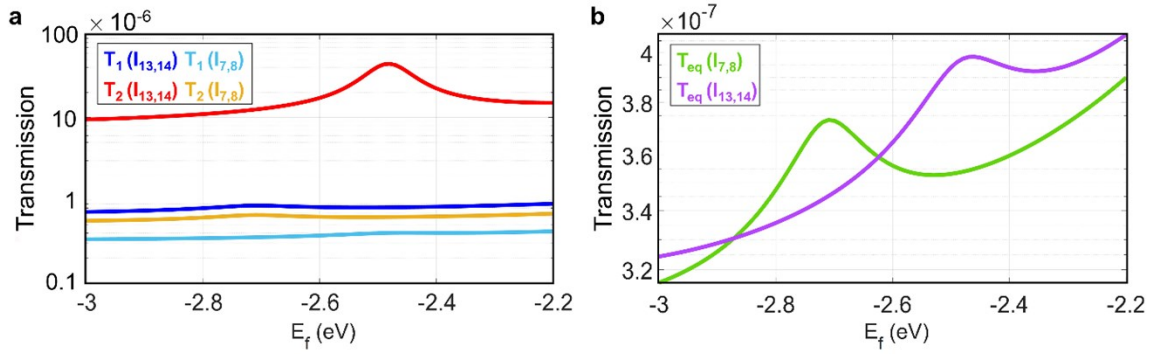

Figure S13. a, Transmission plots of Ox-$I_{13,14}$ and Ox-$I_{7,8}$, showing T_1 and T_2, with $T_2 >> T_1$. **b,** Comparison between T_{eq}, showing that both cases yield similar transmission regardless of the location of Aq.

TwoOx Double Intercalation Sequential Hopping Model

The calculation was also carried out for the two Ox-Aq molecules intercalating the DNA. In the sequential model, this involves three hops to go from the left contact to the right contact (Figure S14):

$$\frac{1}{T_{eq}} = \frac{1}{T_1} + \frac{1}{T_2} + \frac{1}{T_3}.$$

(S11)

The results confirm the length effect on lowering the electronic coupling between the two ox-Aqs, where the induced energy levels are also deep in the BG which isolates them from the molecular

orbitals of the DNA. Indeed, as even though $I_{13,14}$ would have a higher coupling to the right contact, the low coupling between the two Aqs lowers the transmission along the structure. Hence, the lower transmission to/from $I_{7,8}$ results in an equivalent transmission that is comparable to single ox-Aq intercalation as discussed in the main text.
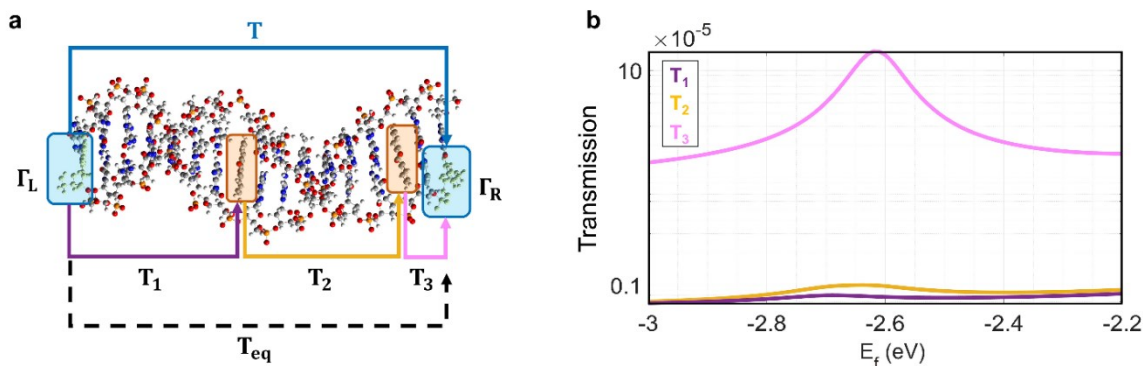

Figure S14. a, Sequential hopping scheme for the two anthraquinone intercalation case, going from leftmost guanine, to the two anthraquinones and exiting through the rightmost guanine. **b** Comparison between T_1, T_2, and T_3, showing distance effect on transmission which causes lower equivalent transmission.

Electron Number Calculation

The electron count is calculated at room temperature, using the same charge transport calculations set up. It is important to mention that since the gold contacts are not explicitly included in the model, the resulting Hamiltonian from DFT calculations that is used in the Green's function (GF) does not yield the exact electron number of the system. Thus, the GF approach requires the Hamiltonian to be updated self-consistently while solving Poisson's equation with the appropriate boundary conditions to account for the contact atoms' effect on the electrostatics, which would yield the accurate electron count. However, in our approach, we are not solving explicitly for the total number of electrons of the system, but rather looking at a smaller energy window (bandgap) to investigate the amount of shift caused by partial charge transfer. Electron count for each case is plotted in Figure S15, where the flat regions resemble the bandgap. We can then find the number of electrons required to go from HOMO to LUMO by following this flat region. The first thing to notice is that for the Ox-Aq (blue, red, and black), sudden jumps are seen in the electron count as

we pass from -3 eV to -2.4 eV. The charge increases by 1 electron (2 electrons for the two Aq case), which is consistent with the location of the LUMO induced by the Aq. As we assume the partial charge transfer to be less than one electron, this limits the energy sweeping for Ox-Aq cases to energies between -4.5 and -3 eV. In this energy window, the electron count increases only by 0.4 electron (0.013 electron/base). As for the Re-Aq cases, they provide a larger bandgap (energy window) for the energy sweep. Therefore, the electron count increases by 0.8 electron (0.027 electron/base) as energy is swept from -4.2 eV to -1.8 eV. As for the bare DNA, 0.73 electron (0.024 electron/base) increase is seen when going from -4.5 eV to -1.5 eV. It is important to note that the values for bare DNA and Re-Aq are to go from HOMO to LUMO, whereas in principal this need not be the case as Fermi energy of the contacts can be assumed to be initially in the middle of the bandgap (around -3 eV). Therefore, we calculate the electron count for energy windows similar to the Ox-Aq cases (from -3 eV to HOMO per case). The calculations show that it will require a smaller amount of charge to go to the vicinity of HOMO (an average of 0.44 electron for Re-Aq cases, and 0.46 electron for ds-DNA). These values are comparable to the literature,[S28] where a thiol-conjugated hexathiophene molecule was shown to have ~0.31 electron charge transfer occurring from the electrode to the molecule. Noting that the hexathiophene has 54 atoms, which can correspond to two DNA nucleotides. And thus, the amount of charge required for our system (0.46-0.4 electron) can be reasonably supplied by the partial charge transfer occurring from gold contacts into the molecule.
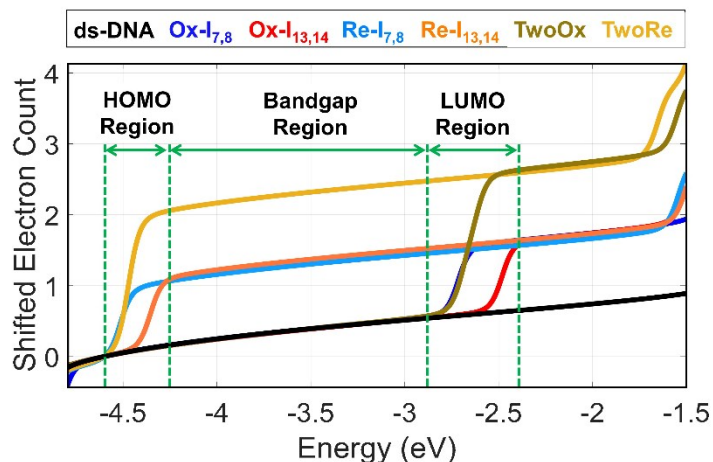

Figure S15. Shifted electron count for each case found by integrating DOS, focused on the bandgap region and the edges of HOMO and LUMO regions.

This difference in electron number within the bandgap region tells us that the amount of molecular orbitals shift is different per case. Thus, making Fermi energy location not necessarily close to HOMO, as was shown in the main text. Figure S16 shows a sample of how dE_i/dN is extracted. The flat region between two peaks resembles the bandgap in which the average value of the inverse plot is taken to extract dE_i/dN.
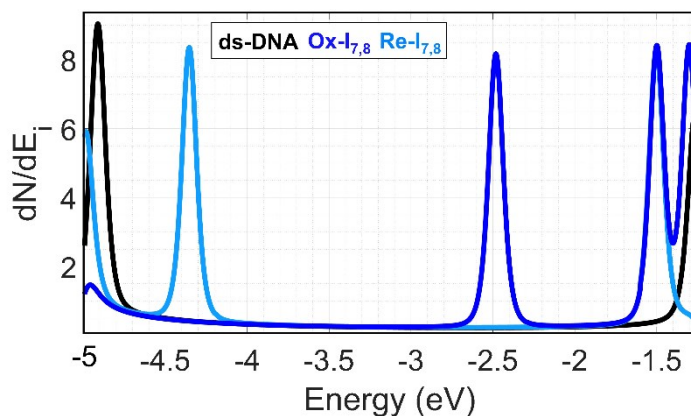

Figure S16. The average rate of change is taken from the flat region between the peaks. The peaks at energy < -4 eV (> -3 eV) resemble the HOMO (LUMO) of the different cases. Only three cases are shown for clarity.

Table S2 summarizes dE_i/dN for the DNA:RNA + intercalator cases. The values follow the same trend of ds-DNA as seen in the main text: Ox-Aq < DNA:RNA

Table S2. Average rate of change in energy with respect to number of electrons for DNA:RNA

Intercalator Molecule	Intercalation Position	dE_i/dN (eV/electron)
Ox-AqNEO	$I_{13,14}$	2.62
Ox-AqNEO	$I_{7,8}$	2.57
Ox-Aq	$I_{13,14}$	2.72
Ox-Aq	$I_{7,8}$	2.66
DNA:RNA	-	2.86

Partial Charge Transfer Sweep

Here, we display the results of estimating the Fermi energy for ds-DNA cases at different initial guesses of E_{f_0} (based on Eq. 2 in the main manuscript). The main condition for dN is to be below 1 electron, and the maximum allowable shift for Ef (from E_{f_0}) is to reach the HOMO of each case. This limits dN to have a maximum corresponding the HOMO of each case (Figure S17).
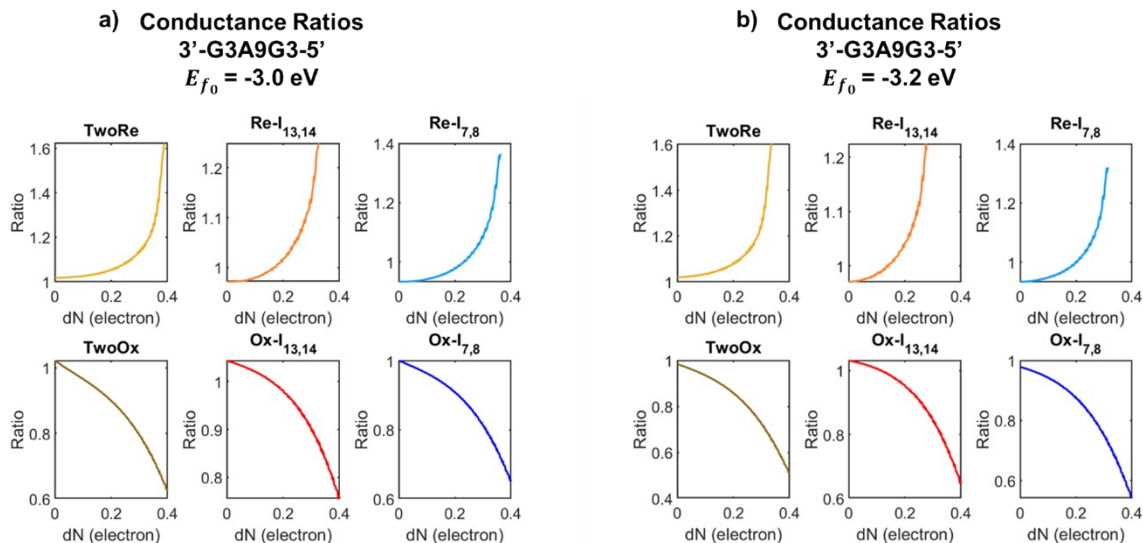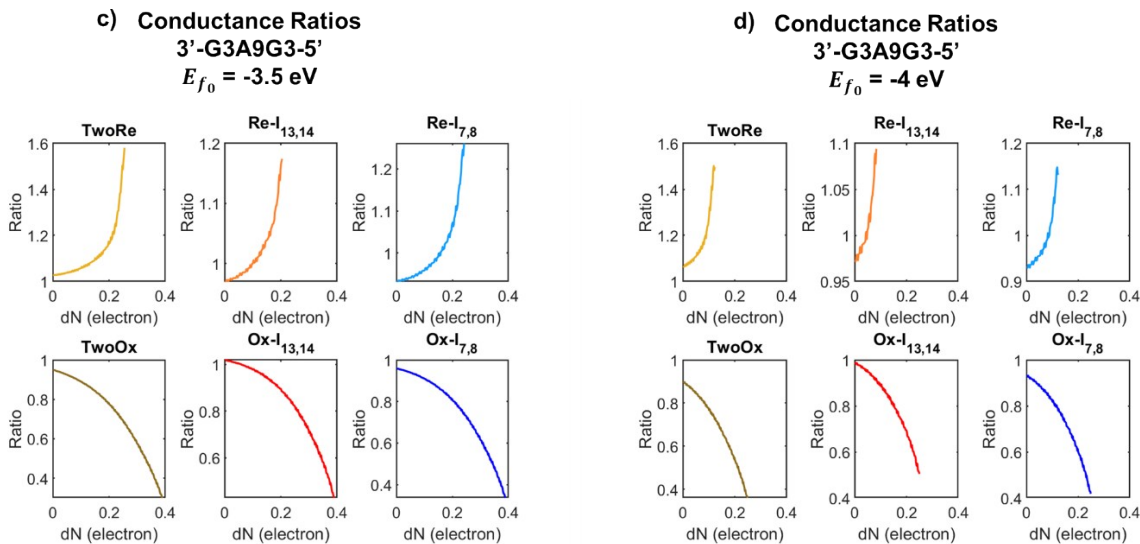
Figure S17. Conductance ratios for the ds-DNA structure (3'-G3A9G3-5') as a function of partial charge transfer at different initial E_{f0}. The cutoff seen in the ratios is due to dN causing the maximum allowable shift to E_{f0} (i.e. E_f= HOMO).

Figure S17 shows that the ratio trend is maintained at various E_{f0}. However, the maximum ratio value decreases at $E_{f0} = -4\ eV$. This result indicates that relatively higher conductance ratios are expected if the initial location of Fermi energy (before the contact-molecule junction is made) was more than 500 meV away from the HOMO region (E_{f0}< -4 eV).

The maximum, minimum, and average conductance for the 3'-G3A9G3-5' strand values are taken for the *dN* sweeps, starting from different E_{f0} and reported in Figure S18.
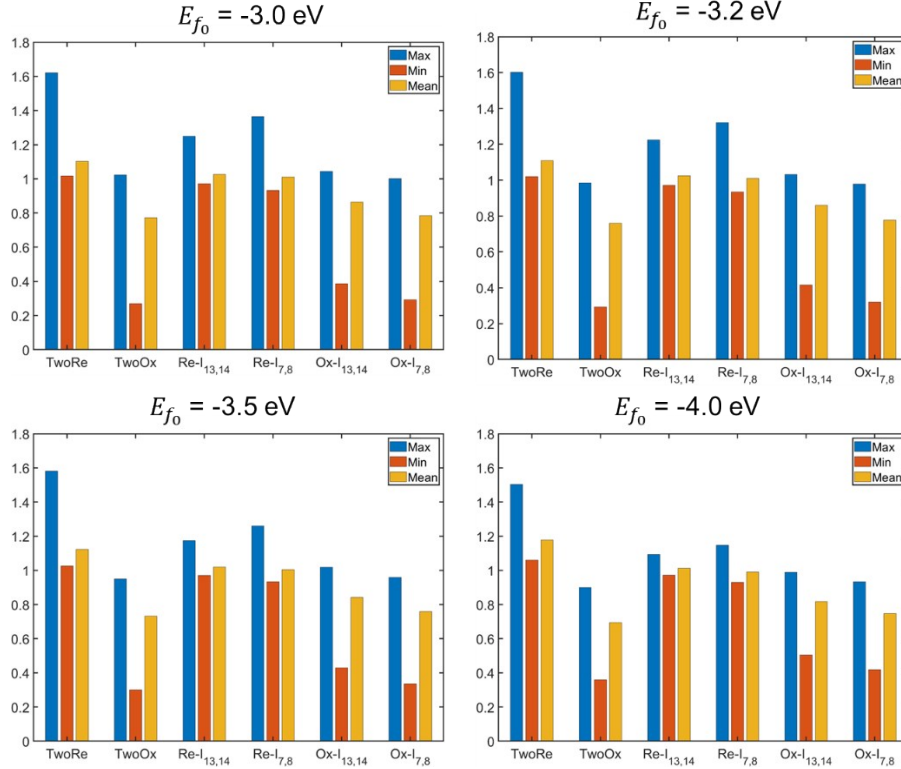
Figure S18. The maximum, minimum, and average conductance for the 3'-G3A9G3-5' strand values are taken for the dN sweeps, starting from different E_{f_0}.

Effect of AT Region Length on Energy Levels

The Aq in $I_{7,8}$ location in the shorter strand (G3A3G3) is equivalent to $I_{13,14}$ in the longer strand (G3A9G3). In the shorter strand, Aq-induced level is now 250 meV away from the HOMO of the DNA as opposed to 650 meV in G3A9G3 (Figure S19).

The structural differences caused by decreasing the length of the helix from 15 base pairs to 9 base pairs may play a role in this variation. Thus, we used X3DNA[S29] to analyze the structural properties of $I_{7,8}$ (G3A3G3) and $I_{13,14}$ (G3A9G3). Since coupling between bases is important in transmission, we focused on the overlap area between adjacent bases which is an indicator of it. Figure S20a shows the overlap area between adjacent bases to the Aq, corresponding to A_6G_7 ($A_{12}G_{13}$ for G3A9G3) and G_8G_9 ($G_{14}G_{15}$ for G3A9G3). Here, we notice that for $I_{7,8}$, the overlap is ~twice as much as the $I_{13,14}$ case. This is further proven by the coupling parameters extracted from the

Hamiltonian (Figure S20b). These observations agree with the literature, as shorter AT regions are found to be the cutoff value for maintaining the electronic coupling between GC base-pairs.[S26, S 27]
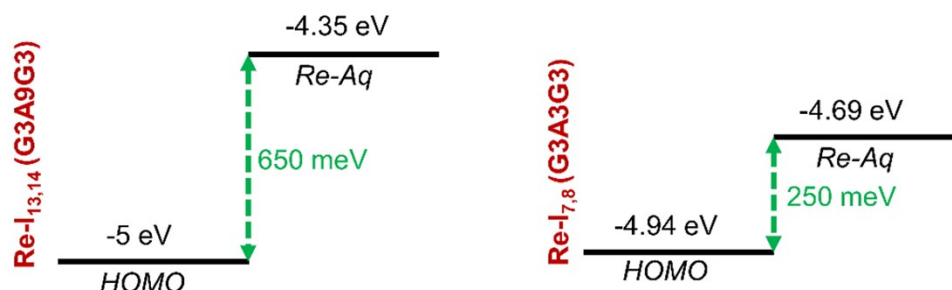

Figure S19. Energy separation between Aq-induced level and nearest HOMO of the DNA. **Left** Longer AT region case. **Right** Shorter AT region case, showing the Aq having a closer HOMO.
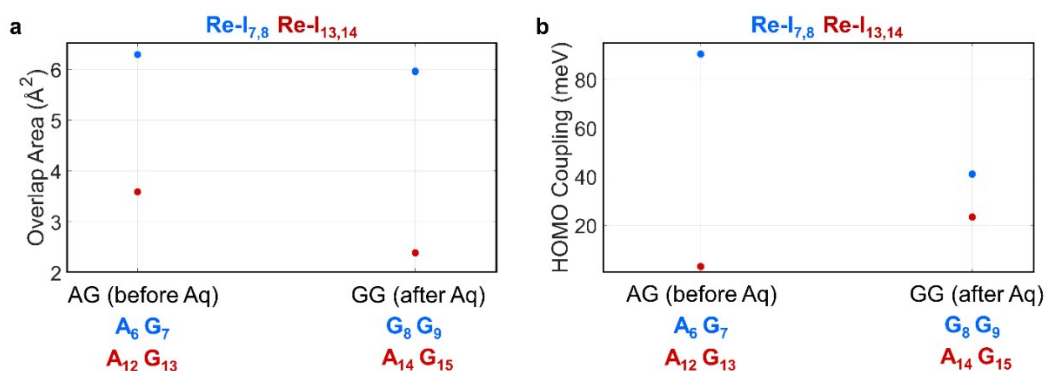

Figure S20. a, Overlap area comparison for $I_{7,8}$ (G3A3G3) (blue) and $I_{13,14}$ (G3A9G3) (red). **b,** HOMO coupling extracted from the Hamiltonian calculated with DFT. The adenine-guanine coupling is higher for the shorter structure.

$I_{5,6}$ Intercalation induced HOMO Shift

The Re-Aq in $I_{5,6}$ location yields a shift in the HOMO of the DNA on the 3'-G2 region, the delocalized HOMO in that region is now at a higher energy level (-4.71 eV) as opposed to the original structure (without intercalation) where the HOMO is at the G3-5' end of the strand (see 2D DOS in Figure S23). This effect is not present in the $I_{7,8}$ of G3A3G3 and can be seen at TwoRe, where $I_{5,6}$ is present simultaneously with $I_{7,8}$.

To understand this, we also used X3DNA to analyze the structural properties of the different cases at the 3'-GGG side of shorter AT structures (in which the HOMO is shifted to higher energy for

$I_{5,6}$). Figure S21 shows the overlap area between adjacent bases for $I_{5,6}$, $I_{7,8}$, and ds-DNA. We notice that both $I_{7,8}$ and ds-DNA have similar trends, whereas $I_{5,6}$ case displays an increase in overlap between C_2C_3 (Figure S21a), and G_1G_2 as well as G_3A_1 as seen in Figure S21b.
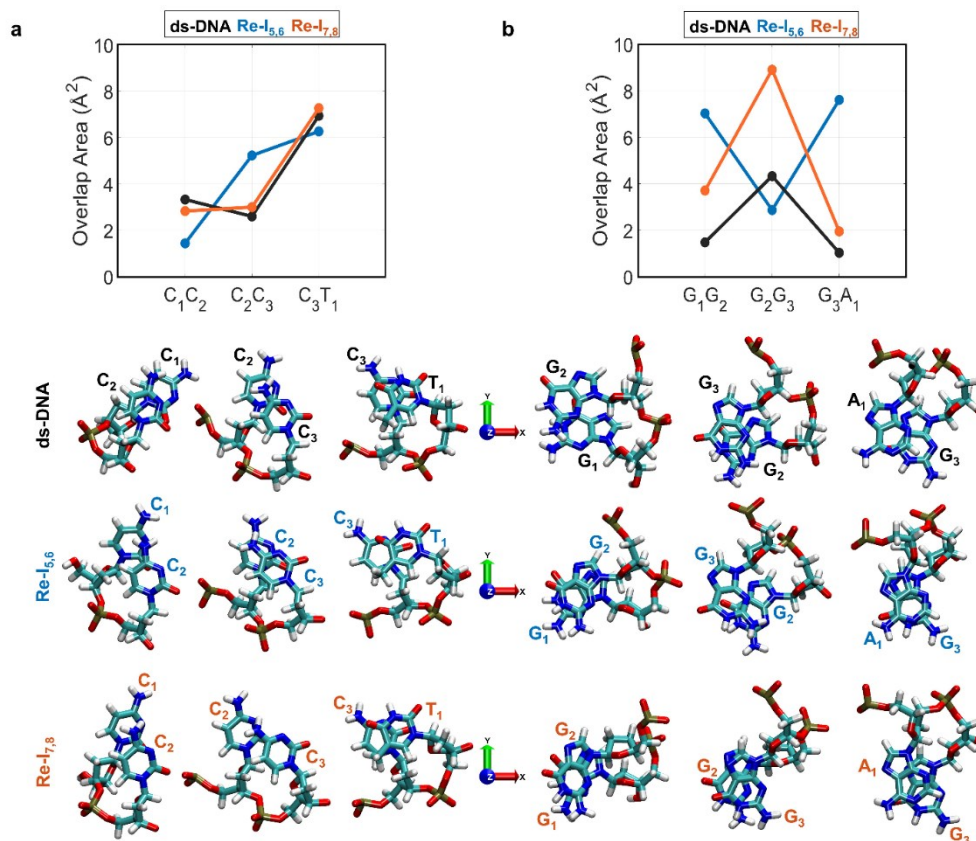

Figure S21. a, Overlap area comparison for 5'-CCT and position of the corresponding bases, **b,** Overlap area comparison for 3'-GGA and position of the corresponding bases.
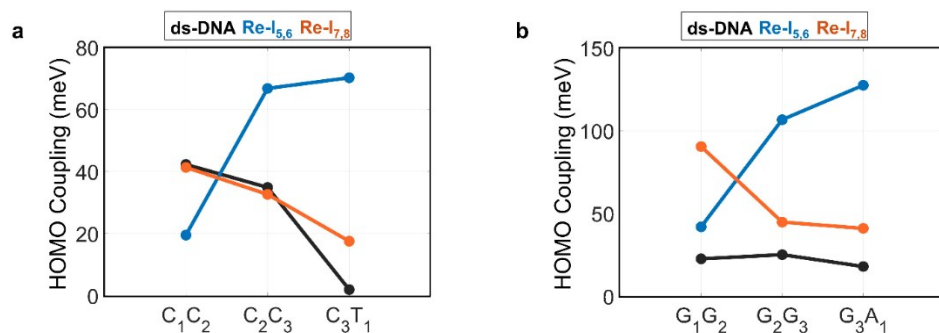
Figure S22. Electronic coupling parameters extracted from the Hamiltonian (off-diagonal elements) at **a,** 5'-CCC and **b,** 3'-GGG. The trends show that $I_{5,6}$ displays higher coupling between the HOMO of the bases near the Aq location.

These results show that the location of intercalation does have a unique impact on the structural properties of the shorter strand, hence increasing the coupling between the neighboring bases on the 3'-end. We also plotted the HOMO coupling for the neighboring bases, further proving that the $I_{5,6}$ causes enhanced electronic coupling (interactions) between the bases of the 3'-end (Figure S22). According to this analysis, we expect that the location of intercalation causes the HOMO to shift to a higher energy state, resulting in a near resonant tunneling with the Aq-induced level, yielding higher transmission (conductance) peak.

The 2D density of states (DOS) (Figure S23), the transmission (Figure S24) and the conductance (Figure S25) plots for G3A3G3 case are given below.
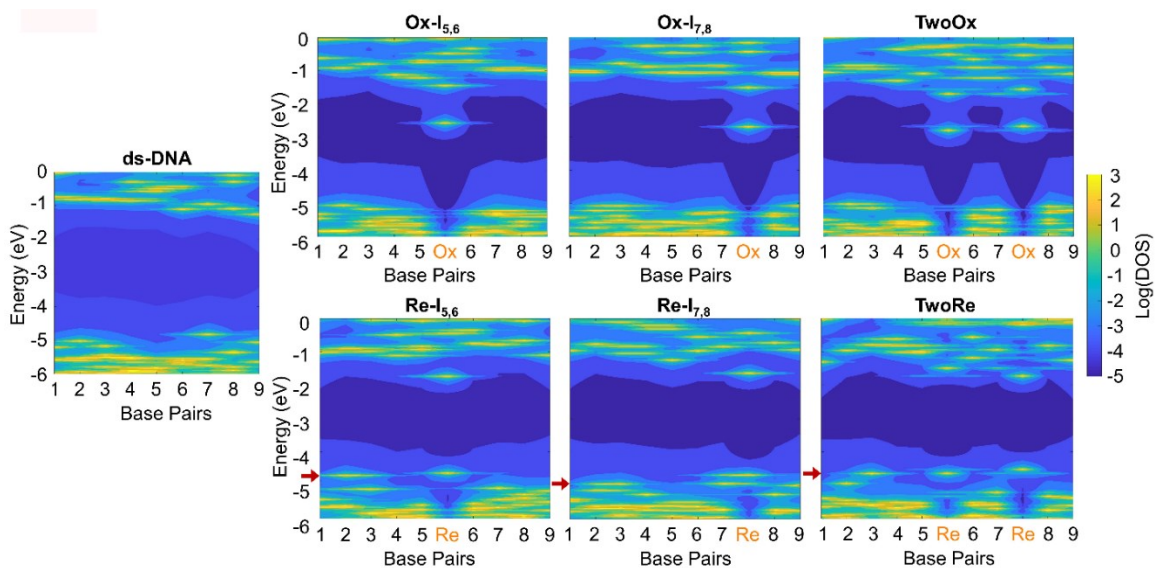

Figure S23. 2D DOS plots for shorter AT region. The induced levels are closer to the molecular orbitals of the DNA than the G3A9G3 case (see the main text Figure 5), with Re-Aq in $I_{5,6}$ causing a noticeable change in HOMO of the DNA (shown with red arrow) on the 3'-GGG side, shifting the delocalized HOMO to be 70 meV from the Aq-induced level. This effect can be seen in the two-Aqs case, but not in the $I_{7,8}$ where Aq is on the other side of the strand (5' end).
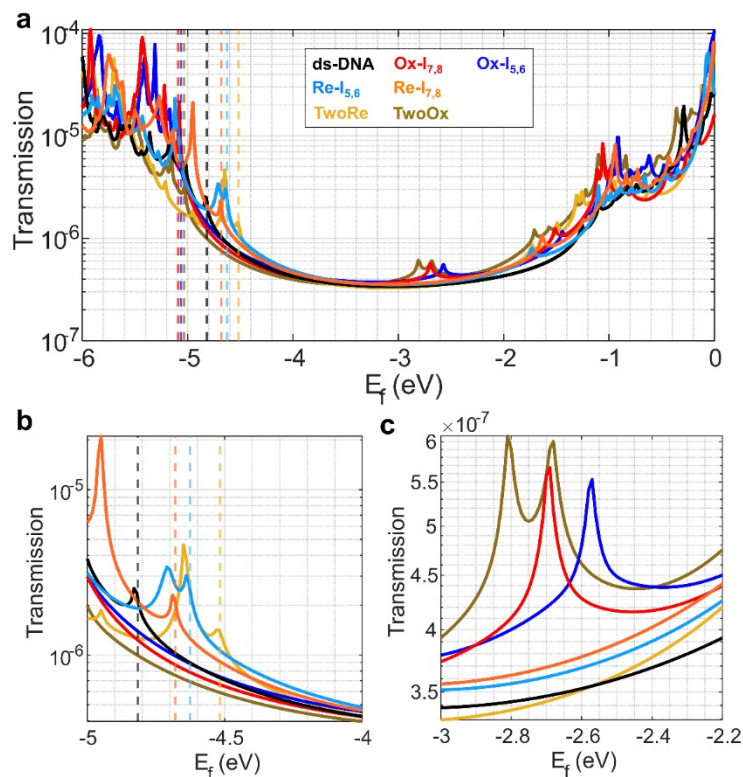
Figure S24. a, Transmission plot for the 3'-G3A3G3-5' strand. **b and c**, show the transmission at the Aq-induced peaks. Re-Aq induced levels increase the transmission by ~3 times compared to DNA at the same energy. Ox-Aq induced levels increase transmission in the bandgap by 56-77% compared to bare DNA, however, the induced levels are unoccupied levels deep in the bandgap region and far away from the expected location of Fermi energy if no gate electrode was applied.
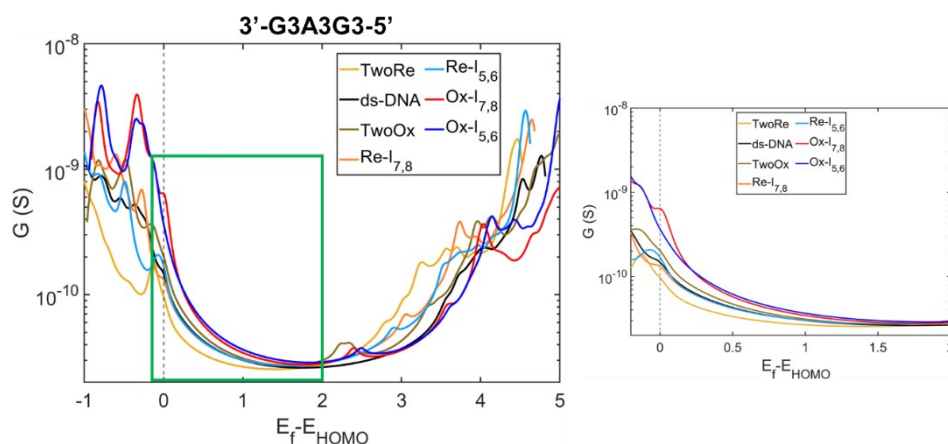

Figure S25. Conductance plot as a function of Fermi energy for 3'-G3A3G3-5' intercalation cases with all HOMOs aligned (dashed line). Inset shows a smaller energy window focused on the HOMO vicinity.

The average rate of change in energy with respect to number of electrons for 3'-G3A3G3-5' are given in Table S3 (see the main text Table 1 for comparison).

Table S3. Average rate of change in energy with respect to number of electrons.

Molecule	dE/dN (eV/electron)	Change
TwoOx	3.62	-0.30
Ox-$I_{7,8}$	3.80	-0.12
Ox-$I_{5,6}$	3.84	-0.08
ds-DNA	3.92	0
TwoRe	5.10	1.18
Re-$I_{5,6}$	5.61	1.69
Re-$I_{7,8}$	5.67	1.75

Figures S26 and S27 show that the ratio trend is maintained at various E_{f_0}. However, the maximum ratio value decreases at $E_{f_0} = -4\ eV$. This result indicates that relatively higher conductance ratios are expected if the initial location of Fermi energy (before the contact-molecule junction is made) was more than 500 meV away from the HOMO region ($E_{f_0} < $ -4 eV).
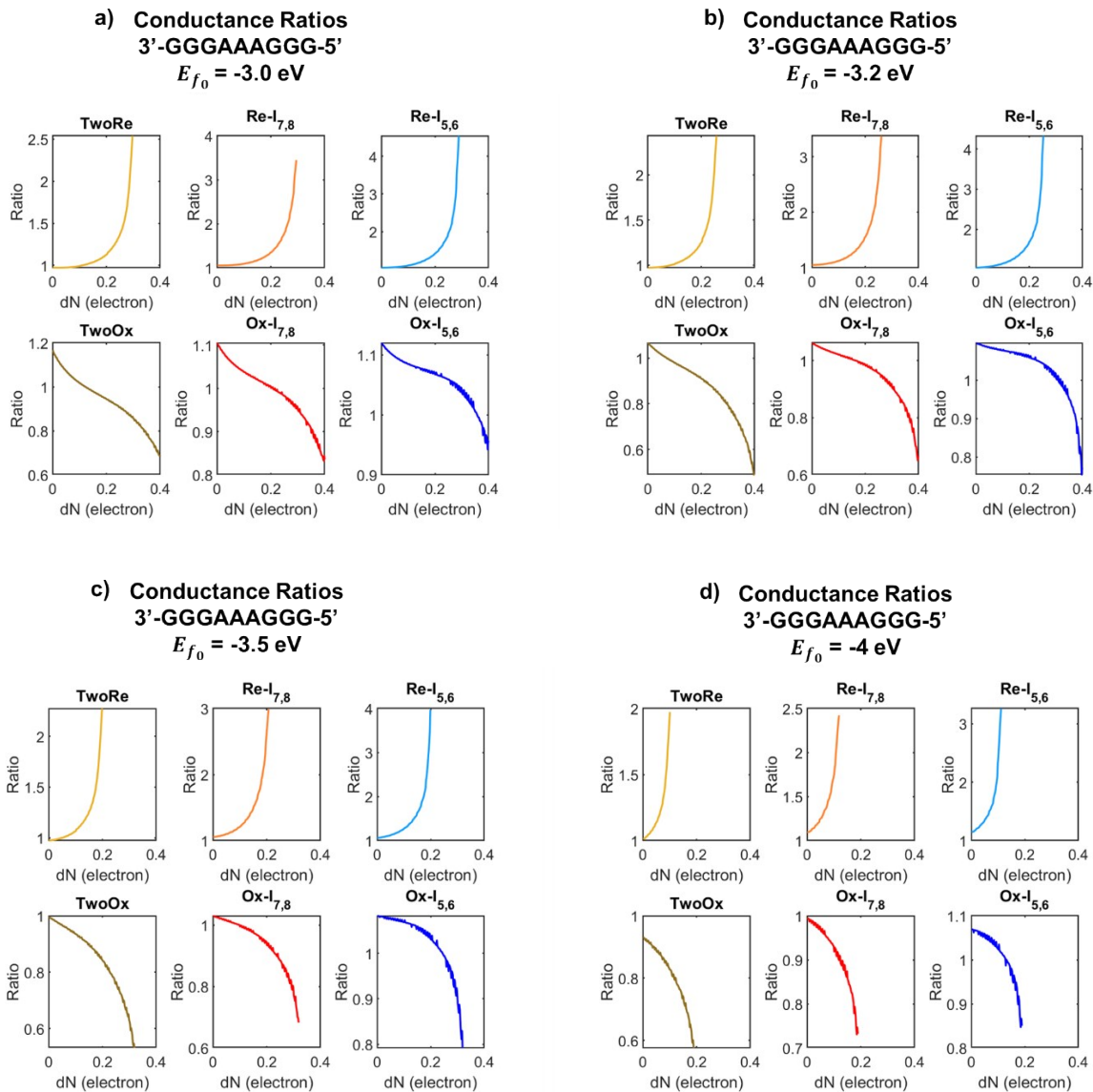
Figure S26. Conductance ratios for shorter structure (3'-GGGAAAGGG-5') as a function of partial charge transfer at different initial E_{f_0}. The cutoff seen in the ratios is due to dN causing the maximum allowable shift to E_{f_0} (i.e. E_f= HOMO).
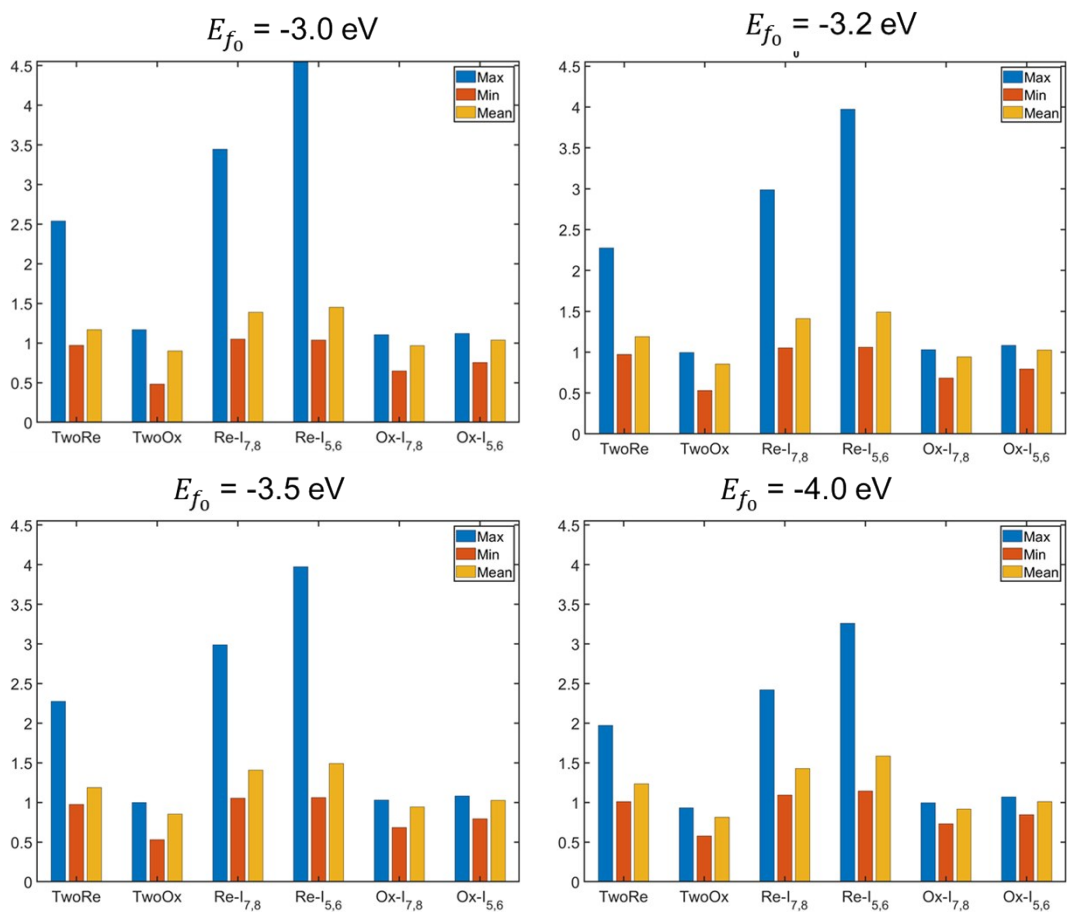
Figure S27 The maximum, minimum, and average conductance for the 3'-G3A9G3-5' strand values are taken for the *dN* sweeps, starting from different E_{f_0}.

References

S1   J. C. Phillips, R. Braun, W. Wang, J. Gumbart, E. Tajkhorshid, E. Villa, C. Chipot, R. D. Skeel, L. Kalé and K. Schulten, *J. Comput. Chem.*, 2005, **26**, 1781–1802.

S2   K. Vanommeslaeghe, E. Hatcher, C. Acharya, S. Kundu, S. Zhong, J. Shim, E. Darian, O. Guvench, P. Lopes, I. Vorobyov and A. D. Mackerell, *J. Comput. Chem.*, 2010, **31**, 671–690.

S3   W. L. Jorgensen, J. Chandrasekhar, J. D. Madura, R. W. Impey and M. L. Klein, *J. Chem. Phys.*, 1983, **79**, 926–935.

S4   D. Beglov and B. Roux, *J. Chem. Phys.*, 1994, **100**, 9050–9063.

S5   T. Darden, D. York and L. Pedersen, *J. Chem. Phys.*, , DOI:10.1063/1.464397.

S6   S. Miyamoto and P. A. Kollman, *J. Comput. Chem.*, 1992, **13**, 952–962.

S7   G. J. Martyna, D. J. Tobias and M. L. Klein, *J. Chem. Phys.*, 1994, **101**, 4177–4189.

S8   D. Cairns, E. Michalitsi, T. C. Jenkins and S. P. Mackay, *Bioorganic Med. Chem.*, 2002, **10**, 803–807.

S9   M. Wilhelm, A. Mukherjee, B. Bouvier, K. Zakrzewska, J. T. Hynes and R. Lavery, *J. Am. Chem. Soc.*, 2012, **134**, 8588–8596.

S10 M. G. Cardozo and A. J. Hopfinger, *Mol. Pharmacol.*, 1991, **40**, 1023–1028.

S11 D. A. Case, V. Babin, J. T. Berryman, *et al.*, *AMBER 14*, 2014.

S12 D. A. Case, R. M. Betz, D. S. Cerutti, *et al.*, *AMBER 16, Univ. California, San Fr.*

S13 A. Pérez, I. Marchán, D. Svozil, J. Sponer, T. E. Cheatham, C. A. Laughton and M. Orozco, *Biophys. J.*, 2007, **92**, 3817–3829.

S14 M. Zgarbová, M. Otyepka, J. Šponer, A. Mládek, P. Banáš, T. E. Cheatham and P. Jurečka, *J. Chem. Theory Comput.*, 2011, **7**, 2886–2902.

S15 I. Ivani, P. D. Dans, A. Noy, A. Pérez, I. Faustino, A. Hospital, J. Walther, P. Andrio, R. Goñi, A. Balaceanu, G. Portella, F. Battistini, J. L. Gelpí, C. González, M. Vendruscolo, C. A. Laughton, S. A. Harris, D. A. Case and M. Orozco, *Nat. Methods*, 2016, **13**, 55–58.

S16 J.-P. Ryckaert, G. Ciccotti and H. J. C. Berendsen, *J. Comput. Phys.*, 1977, **23**, 327–341.

S17 W. Humphrey, A. Dalke and K. Schulten, *J. Mol. Graph.*, 1996, **14**, 33–38.

S18 J. Wang, R. M. Wolf, J. W. Caldwell, P. A. Kollman and D. A. Case, *J. Comput. Chem.*, 2004, **25**, 1157–1174.

S19 M. D. Hanwell, D. E. Curtis, D. C. Lonie, T. Vandermeersch, E. Zurek and G. R. Hutchison,

J. Cheminform., 2012, **4**, 17.

S20 D. J. Frisch, M. J.; Trucks, G. W.; Schlegel, H. B.; Scuseria, G. E.; Robb, M. A.; Cheeseman, J. R.; Scalmani, G.; Barone, V.; Petersson, G. A.; Nakatsuji, H.; Li, X.; Caricato, M.; Marenich, A. V.; Bloino, J.; Janesko, B. G.; Gomperts, R.; Mennucci, B.; Hratch, 2016.

S21 J. Qi, N. Edirisinghe, M. G. Rabbani and M. P. Anantram, *Phys. Rev. B - Condens. Matter Mater. Phys.*, , DOI:10.1103/PhysRevB.87.085404.

S22 H. Kim, M. Kilgour and D. Segal, *J. Phys. Chem. C*, 2016, **120**, 23951–23962.

S23 C. J. O. Verzijl, J. S. Seldenthuis and J. M. Thijssen, *J. Chem. Phys.*, 2013, **138**, 094102.

S24 C. Adessi, S. Walch and M. P. Anantram, *Phys. Rev. B - Condens. Matter Mater. Phys.*, 2003, **67**, 1–4.

S25 H. Mehrez and M. P. Anantram, *Phys. Rev. B - Condens. Matter Mater. Phys.*, 2005, **71**, 115405.

S26 T. Kubař, R. Gutiérrez, U. Kleinekathöfer, G. Cuniberti and M. Elstner, *Phys. Status Solidi Basic Res.*, 2013, **250**, 2277–2287.

S27 B. Jawad, L. Poudel, R. Podgornik, N. F. Steinmetz and W. Y. Ching, *Phys. Chem. Chem. Phys.*, 2019, **21**, 3877–3893.

S28 G. Peng, M. Strange, K. S. Thygesen and M. Mavrikakis, *J. Phys. Chem. C*, 2009, **113**, 20967–20973.

S29 X. J. Lu and W. K. Olson, *Nucleic Acids Res.*, 2003, **31**, 5108–5121.

S30 B. Giese, *Acc. Chem. Res.*, 2000, **33**, 631–636.

S31 Y. Li, L. Xiang, J. L. Palma, Y. Asai and N. Tao, *Nat. Commun.*, 2016, **7**, 1–8.